New indicator for damage localization in a thick adhesive joint of a composite material used in a wind turbine blade

Khoshmanesh, S.; Watson, S. J.; Zarouchas, D.

DOI
10.1016/j.engstruct.2023.115870

Publication date
2023

Document Version
Final published version

Published in
Engineering Structures

Engineering Structures 283 (2023) 115870

Contents lists available at ScienceDirect

Engineering Structures

journal homepage: www.elsevier.com/locate/engstruct

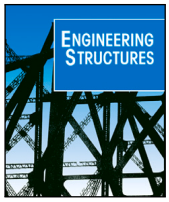

New indicator for damage localization in a thick adhesive joint of a composite material used in a wind turbine blade

S. Khoshmanesh *, S.J. Watson, D. Zarouchas

Faculty of Aerospace Engineering, TU Delft, Kluyverweg 1, 2629 HS Delft., The Netherlands

ARTICLE INFO

Keywords:
Damage localization
Damping
Adhesive joint
Fatigue
Phase of mode shapes

ABSTRACT

In this paper, a new indicator to localize fatigue damage in a fibre glass composite structure, i.e. spar cap to shear web thick adhesive joint of a wind turbine blade, is presented. This indicator is based on the effect of damping on the phase of the mode shapes of the structure. When fatigue damage occurs, damping increases in the defective area and this leads to an increase in the local energy dissipation. This non-uniformity in the energy dissipation throughout the structure causes the structure to vibrate with mode shapes whose structural elements no longer have the same phase creating complex mode shapes. A visco-elastic finite element (FE) vibration model is developed for a thick adhesive joint of a wind turbine blade. The mass, stiffness, and damping matrix extracted from the FE model are used to determine the complex mode shapes. The results show that the damaged area is located where the spatial derivative of the phase of the components of the mode shapes is minimum. Changes in the phase of mode shapes of the structural elements are strongly dependent on the location of damage. In the locations where the strain modal energy is greater, the change in the phase is also higher.

1. Introduction

With the ever-increasing size of wind turbine blades, especially for offshore machines, deploying a suitable condition monitoring system in order to reduce the levelized cost of energy (LCOE) is essential [1]. This is more important for far offshore wind farms which have low accessibility [2]. Four main methods have been proposed for the condition monitoring of a wind turbine blade [3]: vibration-based methods, strain measurements, acoustic emission and ultrasonic wave propagation. For the strain measurements, acoustic emission and the ultrasonic wave propagation methods, sensors should be close to the damage source in order to detect the damage. Therefore, a large number of sensors would need to be installed in different parts of a blade in order to effectively monitor damage, which is an expensive and impractical solution [4].

Vibration-based techniques are easier to implement and are potentially less expensive than other methods. For vibration-based methods, two main techniques are used to detect damage: methods which are based on change in stiffness and those which are based on change in damping [5,6].

For the former, the reduction in natural frequency is used as an indication of reduction in overall stiffness of the structure which in turn is used to infer damage. Increase in the mode shape curvature or decrease in modal strain energy are the most frequent methods which are employed to localize damage. All these proposed techniques rely on the assumption that damage leads to an appreciable reduction in the stiffness of a structure [7,8]. But in a complex composite structure like a wind turbine blade, which consists of several structural elements, such as spar caps, trailing and leading edges, etc, a change in stiffness may not be significant unless severe damage occurs which can compromise the operation of the wind turbine [9].

To identify damage in a wind turbine blade, the latter method described above, namely the detection of changes in the material damping of structure may be a better alternative.

An early experimental investigation to identify damage by measuring the modal damping of a structure was carried out by Modena and Zonta [10,11]. They evaluated the use of modal damping to identify manufacturing defects or structural damage in pre-cast reinforced concrete. In a similar fashion, Kawiecki [12] showed the feasibility of measuring modal damping by using arrays of piezoelectric transducers in a study of two types of concrete blocks. It was found that damping could be a useful property to detect damage in a non-metallic structure. Unlike identification, the localization of damage based on changes in damping is a more complicated challenge. Some researchers have tried to propose a method to localize damage but with limited success. Among these researchers, Keye [13] attempted to localize de-lamination damage in a carbon fibre reinforced polymer

* Corresponding author.
E-mail address: s.khoshmanesh@tudelft.nl (S. Khoshmanesh).

https://doi.org/10.1016/j.engstruct.2023.115870
Received 23 June 2022; Received in revised form 13 January 2023; Accepted 18 February 2023
Available online 27 February 2023

(CFRP) structure by measuring changes in its modal damping and the introduction of a modified modal assurance criterion. Although the concept of change in modal damping as an indicator of damage in CFRP materials was verified, its use regarding damage localization required further work. Montalvao et al. [14] proposed a method to localize damage in a CFRP plate. They combined the change in modal damping factor from a reference state to a damaged state with the modal strain shape to produce a spatial damage index. The significant number of false positive and false negative results were a drawback of this method and further research was suggested to improve the accuracy of the index. Another disadvantage was that this method relies on identifying a large number of mode shapes which makes it of limited practical use.

Compared to metals, composite materials have generally a higher damping capacity. The major reason for this is the visco-elasticity of the polymeric matrix [15]. In fibre-reinforced polymers such as seen in a thick adhesive joint, the dominant damping mechanism is related to the visco-elastic behaviour of the matrix and/or fibre materials. Coulomb friction due to slip in un-bonded regions of the fibre/matrix interface appears to have less influence than visco-elastic effects [16]. Thermo-elastic damping and other mechanisms, such as dislocation damping, are important in metal matrix composites but not in a polymer matrix [16].

To effectively develop a damage model, a model of damping based on the visco-elastic properties of the composite material is considered. In a wind turbine thick adhesive joint, i.e., spar cap to shear web, the adhesively bonded connection is a key element for the structural integrity of the blade. If the joint suffers fatigue damage at the bond-line then this can propagate through the spar cap and lead to delamination and de-bonding of the spar cap from the webs [17,18]. In a previous study, fatigue damage in such a test joint was studied experimentally by assessing the change in the damping properties of the joint material [19].

In this paper, to localize damage in a thick adhesive joint of a composite material used in a wind turbine blade, a new indicator based on the effect of damping on the phase of mode shapes is presented. This approach uses a visco-elastic damping model to develop a finite element (FE) vibration equation. The mass, stiffness and damping matrix extracted from the FE model are used as input parameters to a MATLAB program to find the complex mode shapes. Then the phase of the components of the mode shapes are used to localize damage.

2. Finite element visco-elastic damping model

The visco-elastic behaviour of a composite material is the dominant mechanism for energy dissipation in such a material when subjected to fatigue. Logically, this type of behaviour should be expected for such as a spar cap-shear web thick adhesive joint in a wind turbine blade. Therefore, to investigate the dynamic behaviour of such a structure, a finite element visco-elastic vibration model is used.

Using a finite element framework, the displacement within each element of a structure is expressed in a Lagrangian context as a function of initial position and time, which can be written as [20]:

$$U^e(X,Y,Z,t) = \boldsymbol{N}(X,Y,Z)q^e(t) \tag{1}$$

In this equation, variables with an arrow over the top denote a vector and variables with a bold letter denote a matrix or tensor. X, Y and Z are the initial position of elements in the structure and $U^e(X,Y,Z,t)$ is the displacement vector for each element within the structure. $\boldsymbol{N}(X,Y,Z)$ is the shape function matrix and is dependent on the type of each element. $q^e(t)$ is the nodal displacement vector whose initial position $q^e(t=0)$ is known but its change in position with time needs to be calculated.

For a linear visco-elastic material, the constitutive equation for the stress–strain relationship at time t can be written as: [21,22]:

$$\boldsymbol{\sigma}(t) = \boldsymbol{C}(t)\epsilon(0) + \int_0^t \boldsymbol{C}(t-\tau)\dot{\epsilon}(\tau)d\tau \tag{2}$$

where $\dot{(\cdot)}$ represents the time derivative operator:

$$\dot{(\cdot)} = \partial()/\partial(t) \tag{3}$$

τ is the characteristic relaxation time and $\boldsymbol{C}(t)$ is the visco-elastic fourth order tensor of the material properties which due to the symmetry of the stress and strain can be represented in Voigt notation as a 6×6 dimension matrix. The strain $\epsilon(t)$ and stress $\boldsymbol{\sigma}(t)$ are second-order tensors which due to symmetry can also be expressed in Voigt notation as 6×1 vectors [20].

$$\sigma = \begin{Bmatrix} \sigma_x \\ \sigma_y \\ \sigma_z \\ \sigma_{xy} \\ \sigma_{yz} \\ \sigma_{xz} \end{Bmatrix} \quad , \quad \epsilon = \begin{Bmatrix} \epsilon_x \\ \epsilon_y \\ \epsilon_z \\ \epsilon_{xy} \\ \epsilon_{yz} \\ \epsilon_{xz} \end{Bmatrix} \tag{4}$$

In contrast to an elastic material, for a visco-elastic material, $\boldsymbol{C}(t)$ varies with time. The weak form equation of motion for the structure can be derived by applying the principle of virtual work for each element of a structure. This states that for a structure in dynamic equilibrium, the work of the applied forces (including the inertia force) on the structure due to a small deviation, δU, from the equilibrium position is zero. Applying this principle for each element [20], this gives:

$$\int_{V_e} \ddot{U}^T \delta U \rho dV + \int_{V_e} \sigma^T \delta\epsilon dV + \int_{V_e} t^T \delta U \rho dV + \int_{V_e} f^T \delta U \rho dV = 0 \tag{5}$$

The first term is work due to inertial forces within the volume of an element, the second term is work due to stresses within an element, the third term is work due to boundary (non-gravitational external) forces over the surface of an element and the last term is work due to gravitational forces within an element. These terms are for a small displacement of a structure δU from time t to time $t+\delta t$. t is the boundary force per unit area for an element and f is the gravitational force per unit volume of an element. The subscript e indicates that a vector or matrix belongs to an element e of the structure and the superscript T indicates the transpose of a vector or matrix. From Eq. (1):

$$\delta U^e = \boldsymbol{N}\delta q^e \tag{6}$$

Strain in a structure can be related to the displacement field as:

$$\epsilon = \boldsymbol{D}U \tag{7}$$

where $\boldsymbol{D}$ is the operator matrix which acts on the shape function and its form and components depend on the element type and selected solution. From Eqs. (1) and (7):

$$\epsilon = \boldsymbol{D}\boldsymbol{N}q^e \tag{8}$$

$$\delta\epsilon = \boldsymbol{D}\boldsymbol{N}\delta q^e \tag{9}$$

$$\dot{\epsilon} = \boldsymbol{D}\boldsymbol{N}\dot{q}^e \tag{10}$$

The matrix $\boldsymbol{B}$ is then defined as $\boldsymbol{B} = \boldsymbol{D}\boldsymbol{N}$. By substitution of Eqs. (8)–(10) into Eq. (5) and after some manipulation, the finite element form of the equation of motion for an element of the structure is obtained:

$$\boldsymbol{M}^e\ddot{q}^e + q^e(0)\boldsymbol{K}^e(t) + \int_0^t \boldsymbol{K}^e(t-\tau)\dot{q}^e d\tau = F^e \tag{11}$$

where the element mass and stiffness matrices and the force vector are defined as:

$$\boldsymbol{M}^e = \int_{V_e} \boldsymbol{N}^T\boldsymbol{N}\rho dV \tag{12}$$

$$\boldsymbol{K}^e = \int_{V_e} \boldsymbol{B}^T\boldsymbol{C}(t)\boldsymbol{B}\rho dV \tag{13}$$

$$F^e = \int_{V_e} \boldsymbol{N}^T t ds + \int_{V_e} \boldsymbol{N}^T f dV \tag{14}$$

Applying the virtual work principle for all elements and then assembling the mass, stiffness and force vector for the whole structure gives:

$$\boldsymbol{M}\ddot{q} + q(0)\boldsymbol{K}(t) + \int_0^t \boldsymbol{K}(t-\tau)\dot{q}d\tau = F \tag{15}$$

where $\boldsymbol{M}$, $\boldsymbol{K}(t)$ and F are mass and stiffness matrices and force vector for the whole structure, respectively. Eq. (15) in the Laplace domain can be written as:

$$s^2\boldsymbol{M}\bar{q}(s) + s\boldsymbol{K}(s)\bar{q}(s) = F(s) \tag{16}$$

Note that when the Laplace transform is taken, the transformed second term in Eq. (15) is cancelled out by a component of the transformed third term. For a visco-elastic material, the relaxation matrix properties $\boldsymbol{C}(t)$ can be written as the sum of an equilibrium part and a time-dependent part:

$$\boldsymbol{C}(t) = \boldsymbol{C}^0 + \boldsymbol{h}(t) \tag{17}$$

where $\boldsymbol{C}^0$ is the matrix of relaxation properties as $t \rightharpoonup \infty$.

Substituting Eq. (17) into Eq. (13) gives:

$$\boldsymbol{K}^e = \int_{V_e} \boldsymbol{B}^T\boldsymbol{C}^0\boldsymbol{B}\rho dV + \int_{V_e} \boldsymbol{B}^T\boldsymbol{h}(t)\boldsymbol{B}\rho dV \tag{18}$$

By introducing the terms: $\boldsymbol{K}^{0e} = \int_{V_e} \boldsymbol{B}^T\boldsymbol{C}^0\boldsymbol{B}\rho dV$ and $\boldsymbol{H}^e(t) = \int_{V_e} \boldsymbol{B}^T\boldsymbol{h}(t)\boldsymbol{B}\rho dV$ then:

$$\boldsymbol{K}^e(t) = \boldsymbol{K}^{0e} + \boldsymbol{H}^e(t) \tag{19}$$

In the Laplace form:

$$s\bar{\boldsymbol{K}}^e(s) = \boldsymbol{K}^{0e} + s\bar{\boldsymbol{H}}^e(s) \tag{20}$$

where $s\bar{\boldsymbol{K}}^e$, $\boldsymbol{K}^{0e}$ and $s\bar{\boldsymbol{H}}^e(s)$ are the dynamic modulus, storage modulus and loss modulus matrix for an element of structure, respectively. Note that $\boldsymbol{K}^{0e}$ is a constant. By introducing, $\bar{\boldsymbol{D}}^e(s) = s\bar{\boldsymbol{H}}^e(s)$ and substituting Eq. (20) into the Laplace form of Eq. (11) and then assembling the mass, stiffness and force vector for the whole structure, gives:

$$s^2\boldsymbol{M}\bar{q}(s) + \boldsymbol{K}^0\bar{q}(s) + \bar{\boldsymbol{D}}(s)\bar{q}(s) = F(s) \tag{21}$$

This is the Laplace form of the equation of motion where $\boldsymbol{M}$ is the mass matrix, $\boldsymbol{K}^0$ is the stiffness matrix and $\bar{\boldsymbol{D}}(s)$ is the damping matrix. This equation is used to extract complex eigenvalues and complex mode shapes as explained in Section 3.5.

3. Methodology

3.1. Description

A wind turbine blade consists of aerodynamic shells (the pressure side and suction side) and shear webs which are moulded separately and then bonded together in an assembly process using a structural adhesive. The load carrying parts of the shells (spar caps) are constructed from uni-directional composite laminates such as thick GFRM (glass fibre-reinforced materials) [23,24]. Shear webs are built from multi-axial fibre lay-ups and a core of balsa wood or polyvinyl chloride (PVC) foam. The web body is produced by infusion of a balsa/foam core with thin skin laminates, whereas the web foot is primarily made of multi-axial direction glass fibres. The spar-web adhesive joint is manufactured by bonding the web foot onto the spar cap of the blade as shown in Fig. 1.

This web adhesive joint is a key element for the structural integrity of the blade. If the joint suffers fatigue damage at the bond-line then this can propagate through the spar cap and lead to de-lamination and de-bonding of the spar cap from the webs [17].

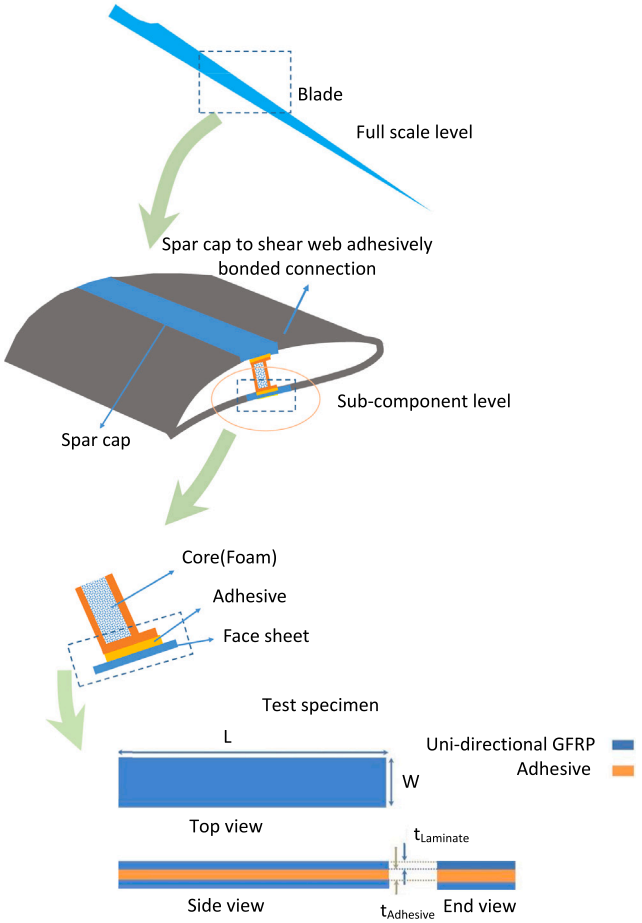

Fig. 1. Schematic illustration of a spar cap-shear web assembly of a wind turbine blade.

3.2. Modelling

A test specimen representative of the spar cap to shear web adhesively bonded connection as shown in Fig. 1 is used for the simulation of damage in this study. This thick adhesive joint consists of two skins of unidirectional fibre glass laminate which are bonded together by means of an adhesive. To study the theoretical response of this joint under varying levels of damage, a model of this joint, shown schematically in Fig. 2, is used. Material properties and dimensions of this joint are given in Table 1. E, G, ν and ρ are Young's modulus, shear modulus, Poisson ratio and density. The index x and y are pointed out to the directions in a Cartesian coordinate system as shown in Fig. 2.

For the purposes of the vibration analysis, the adhesive joint is considered as a solid structure consisting of solid type elements and fixed at one end as shown in Fig. 3 modelled in 3D using ANSYS Structural Analysis 18.2 FE software. To identify and localize damage, the mass, stiffness and damping matrix are extracted. These matrices are used as input to a MATLAB code to calculate the complex mode shapes and the phase of the components of the mode shapes.

3.3. Damage simulation

The damage in this study is simulated within a small section (some elements) of the modelled adhesive joint by changes to the damping properties. This approach was justified by a number of fatigue tension tests conducted in a previous study by the authors [19]. During this

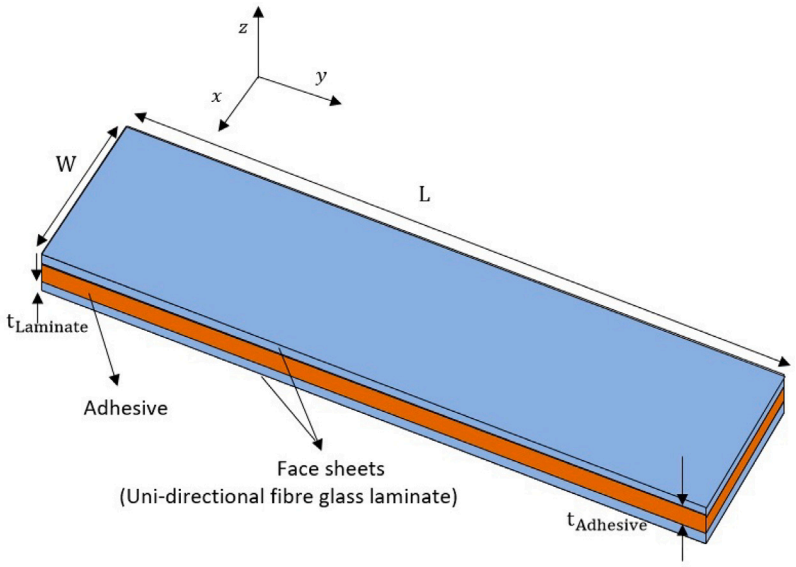

Fig. 2. Schematic illustration of the spar cap-shear web thick adhesive joint modelled in this study.

Table 1
Material properties and dimensions of the thick adhesive joint modelled in this study.

Parts	Material specification		E_Y(Gpa)	E_x(Gpa)	G_{x-y}(Gpa)	ν_{xy}	ν_{yz}	$\rho(g/cm^3)$	L/W/t(cm)
Adhesive	Resin	Epoxy Epikote Resin MGSBPR135G2	5.2	5.2	2.03	0.35	0.35	1.1	37.5/3.6/0.5
	Curing agent	Epoxy Epikure Curing Agent MGS BPH1355G							
Face sheets	Uni-directional fibre glass laminate		31.5	5	3.8	0.4	0.3	1.6	37.5/3.6/0.25

study, changes to the stiffness and damping of several test specimens were measured. The tests showed that the damping experienced a significant change over the lifetime but changes to the stiffness were relatively small. Based on [19], the overall loss factor or modal damping of the same test specimen during a fatigue test increased by 110%–120%. If the damage is localized, the change in the loss factor of the damaged elements is much higher than the overall loss factor or modal damping. Different levels of damage intensity for damaged elements are considered and the highest level is assumed to cause an increase of 110%–120% in modal damping.

Damping is introduced at some elements of the modelled adhesive joint by adjusting the parameters of the Young's (shear) modulus, which is assumed to be dynamic:

$$E(t) = E^0 + h(t) \tag{22}$$

where E^0 is a fixed term (the relaxation modulus) and $h(t)$ is a time-varying term. In the Laplace domain, this equation can be written as:

$$s\bar{E}(s) = E^0 + s\bar{h}(s)E^0 \tag{23}$$

where $s\bar{E}(s)$, E^0, $s\bar{h}(s)E^0$ and $s\bar{h}(s)$ are the dynamic, storage modulus, loss modulus and loss factor of the visco-elastic material, respectively [21]. An expression for the loss factor introduced by McTavish et al. [21] (also known as the Golla–Hughes–McTavish or GHM model) is given by:

$$s\bar{h}(s) = \alpha \frac{s(s + 2\zeta\bar{\omega})}{(s^2 + 2\zeta\bar{\omega}s + \bar{\omega}^2)} \tag{24}$$

where α, ζ and $\bar{\omega}$ are model parameters. Eq. (23) can also be written as:

$$s\bar{E}(s) = E^0 + \eta(s)E^0 \tag{25}$$

Where $\eta(s)$ is the material loss factor. For the damaged section, the damage intensity level (DIL) is defined as:

$$DIL = \frac{\eta_d}{\eta} \tag{26}$$

where η_d is the loss factor for the damaged section. The data in Table 1 are used for the storage modulus. The loss modulus is calculated by multiplying the loss factor by the storage modulus. Using these values as input to ANSYS Structural Analysis 18.2 FE software, the mass matrix $\boldsymbol{M}$, stiffness matrix $\boldsymbol{K}^0$ and damping matrix $\bar{\boldsymbol{D}}(s)$ from Eq. (21) at range of frequencies were extracted.

3.4. Damage identification and localization

The approach proposed in this work for damage localization is based on the premise that damage in a certain part of a composite structure leads to a substantial localized increase in damping (non-proportionality). This local damage creates non-proportionality in the energy dissipation throughout the structure. This means that in the damaged area, the dissipation of energy due to damping is greater compared with the case when there is no damage. This non-proportionality in energy dissipation affects the phase of the characteristic mode shapes of the structure. If the adhesive joint is considered as a number of solid elements supported at one end as shown in Fig. 3, then the kth eigenvector (mode shape) of the structure can be written as:

$$\phi^{(k)} = \begin{Bmatrix} \phi_1^{(k)} \\ \dots \\ \phi_i^{(k)} \\ \dots \\ \dots \\ \phi_n^{(k)} \end{Bmatrix}, \tag{27}$$

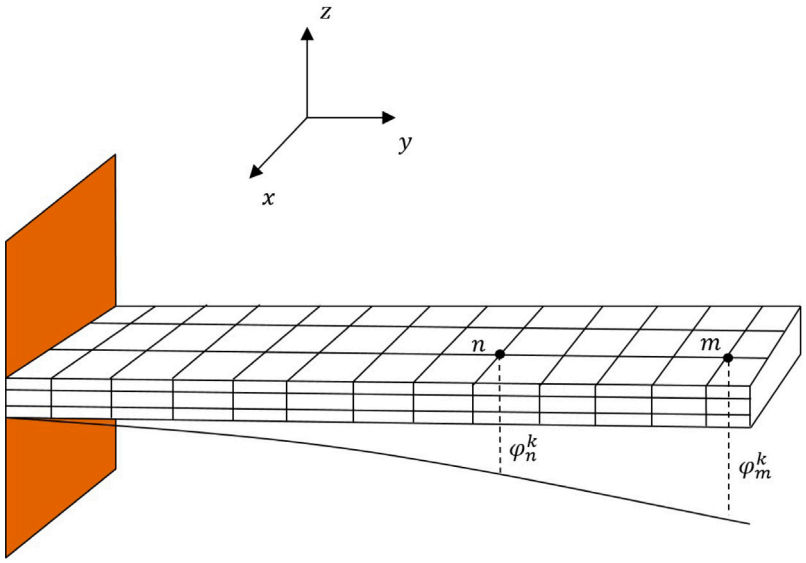

Fig. 3. Schematic illustration of the thick adhesive joint in first bending mode.

where $\phi_i^{(k)}(i = 1, 2, \dots, n)$ are the components or structural element displacements of each mode shape k. The components of the eigenvector are complex and can be written as:

$$\phi_i^{(k)} = \|\phi_i^{(k)}\| e^{j\theta_i^{(k)}},\ i=1,2,\dots,n \tag{28}$$

where $\|\phi_i^{(k)}\|$ is the magnitude and $\theta_i^{(k)}$ is the phase of the ith component of the kth eigenvector and $j = \sqrt{-1}$.

When there is no damage, the dissipation of energy is proportional throughout the structure and the phases of the components of each eigenvector are zero ($\theta_i^{(k)} = 0, i = 1, 2, \dots, n$), [25]. When there is damage in a certain part of the structure, this results in phase differences between the components of the eigenvector especially for those nodes close to the area of damage.

To localize damage, the phases of the complex mode shapes (θ) are calculated. When local damage occurs in a structure, the damping matrix is non-proportional and the eigenvectors are complex. The method used here to calculate the complex eigenvectors is based on expressing each complex mode shape (complex eigenvector) as a linear combination of normal modes and then using a Neumann expansion method to find the vector coefficients.

To identify damage, modal damping is calculated and an increase in modal damping is taken as an indication of damage in the structure. The complex natural frequency of mode k, as denoted by λ_k, can be written:

$$\lambda_k = -R_k + jI_k \tag{29}$$

Where R_k is the real part and I_k is the imaginary part of complex natural frequency for the kth mode. The complex natural frequency λ_k is related to the eigenvalue, s_k:

$$\lambda_k = js_k \tag{30}$$

The magnitude of the complex natural frequency and the modal damping are denoted by ω_k and ζ_k, respectively, and are determined using [26]:

$$\omega_k = \sqrt{R_k^2 + I_k^2} \tag{31}$$

$$\zeta_k = -I_k/\omega_k \tag{32}$$

Substituting Eq. (31) and (32) into Eq. (29) gives an expression for the complex natural frequency:

$$\lambda_k = \omega_k(\sqrt{1-\zeta_k^2} - j\zeta_k) \tag{33}$$

3.5. Calculation of complex eigenvalues and eigenvectors

For a non-proportional damped system with n degrees of freedom, each mode shape of this system is a linear vector composition of n un-damped mode shapes [27]:

$$\phi^{(k)} = \sum_{i=1}^{n} \alpha_i^{(k)} b^{(i)} \tag{34}$$

where $\phi^{(k)}$ is the eigenvector of the kth mode of the non-proportional damped structure, $b^{(i)}$ is the eigenvector of the ith mode of the un-damped structure and $\alpha_i^{(k)}$ is a constant. To calculate the coefficients of Eq. (34), this equation can be substituted into Eq. (21), with $F(s) = 0$, [28]. The left hand side of this equation is then multiplied by the transpose of the mth mode shape, $(b^{(m)})^T$, and using the orthogonal properties of the un-damped mode shapes:

$$\alpha_m^{(k)} s_k^2 + \alpha_m^{(k)} \omega_k^2 + \alpha_k^{(k)} K_{mk} + \alpha_m^{(k)} K_{mm} + \sum_{i=1, i\neq k, i\neq m}^{n} \alpha_i^{(k)} K_{mi} = 0 \tag{35}$$

where

$$K_{mi} = (b^{(m)})^T \bar{\boldsymbol{D}}(s = s_k)\, b^{(i)} \tag{36}$$

Without loss of generality, $\alpha_k^{(k)}$ is considered equal to 1 and Eq. (35) can be rewritten as:

$$\alpha_m^{(k)}\left(\frac{s_k^2 + \omega_m^2 + K_{mm}}{-1}\right) - \sum_{i=1, i\neq k, i\neq m}^{n} \alpha_i^{(k)} K_{mi} = K_{mk} \tag{37}$$

In matrix form, this equation can be written as (see [28]):

$$[P_k - Q_k]A_k = B_k \tag{38}$$

where P_K, Q_K and A_K are given in Box I. The kth row and column of the matrices correspond to the coefficients $\alpha_k^{(k)}$ which are assumed to be known ($\alpha_k^{(k)}$=1), so are removed to give a solution for coefficients other than $\alpha_k^{(k)}$.

Using the Neumann expansion method, the coefficients matrix for kth mode shape can be written as:

$$A_k = [I_{N-1} + R_k + R_k^2 + R_k^3 + \cdots]A_0 \tag{42}$$

where,

$$R_k = P_k^{-1} Q_k \tag{43}$$

$$A_0 = P_k^{-1} B_k \tag{44}$$

$$P_k = \begin{bmatrix} \frac{s_k^2+K_{11}+\omega_k^2}{-1} & 0 & \dots & (k^{th}\text{ term deleted}) & 0 & 0 \\ 0 & \frac{s_k^2+K_{22}+\omega_k^2}{-1} & 0 & & \dots & 0 \\ \dots & \dots & \dots & & \dots & \dots \\ (k^{th}\text{ term deleted}) & & & (k^{th}\text{ term deleted}) & & (k^{th}\text{ term deleted}) \\ 0 & 0 & 0 & & \dots & 0 \\ 0 & 0 & 0 & (k^{th}\text{ term deleted}) & \dots & \frac{s_k^2+K_{nn}+\omega_k^2}{-1} \end{bmatrix} \tag{39}$$

$$Q_k = \begin{bmatrix} 0 & K_{12} & .... & (k^{th}\text{ term deleted}) & \dots & K_{1n} \\ K_{21} & 0 & \dots & & & \\ \dots & \dots & .... & & \dots & \dots \\ (k^{th}\text{ term deleted}) & & & (k^{th}\text{ term deleted}) & & (k^{th}\text{ term deleted}) \\ \dots & \dots & \dots & & \dots & \dots \\ K_{1n} & K_{2n} & \dots & (k^{th}\text{ term deleted}) & \dots & 0 \end{bmatrix} \tag{40}$$

$$A_k = \begin{bmatrix} \alpha_1^{(k)} \\ \alpha_2^{(k)} \\ .. \\ (k^{th}\text{ term deleted}) \\ ..... \\ \alpha_n^{(k)} \end{bmatrix}, B_k = \begin{bmatrix} K_{1k} \\ K_{2k} \\ \dots \\ (k^{th}\text{ term deleted}) \\ \dots \\ K_{nk} \end{bmatrix} \tag{41}$$

Box I.

To solve the matrix form of Eq. (38), an initial guess is made for the kth eigenvalue, for example, by setting $m = k$ in Eq. (35). Knowing that $\alpha_k^k = 1$, then this equation can be rewritten as:

$$s_k^2 + \theta_k + \omega_k^2 = 0 \tag{45}$$

where:

$$\theta_k = K_{kk} + (B_j)^T A_j \tag{46}$$

Then,

$$s_k = -\theta_k + i\sqrt{(4\omega_k^2 - \theta_k^2)} \tag{47}$$

For the first guess, the term $(B_j)^T A_j$ is neglected. The algorithm used to find the complex mode shapes is summarized in Fig. 4.

4. Results

Damage was simulated by varying the material loss factor in four different locations of the thick adhesive joint. Then the effect of damage on the phase angle of motion of the structural elements was investigated for different mode shapes. The four locations were at 2.5%, 10%, 20% and 40% of the length of the joint from the fixed end, denoted as Damage Cases 1–4, respectively. Damage intensity levels (DILs) were identified by the ratio of the loss factor of the damaged area (η_d) to the loss factor of the healthy area (η), i.e., η_d/η. The thick adhesive joint was divided into 248 elements, of which 12 elements were considered as damaged.

4.1. Effect of damage location on the phase of mode shapes

The effect of damage on the phase angle of motion of the structural elements of the first mode shapes for Damage Case 1 was determined and the results are shown in Fig. 5. The natural frequencies of the test specimen for Damage Case 1 and DLI = 2.5 for the first, second, and third modes are 49.272, 95.38, and 305.44 Hz, respectively. To ensure convergence, the number of elements in the test specimens was increased until the natural frequencies did not change. This was achieved when the total number of elements in the test specimen was 744 and changes in natural frequency were less than 0.001%. The

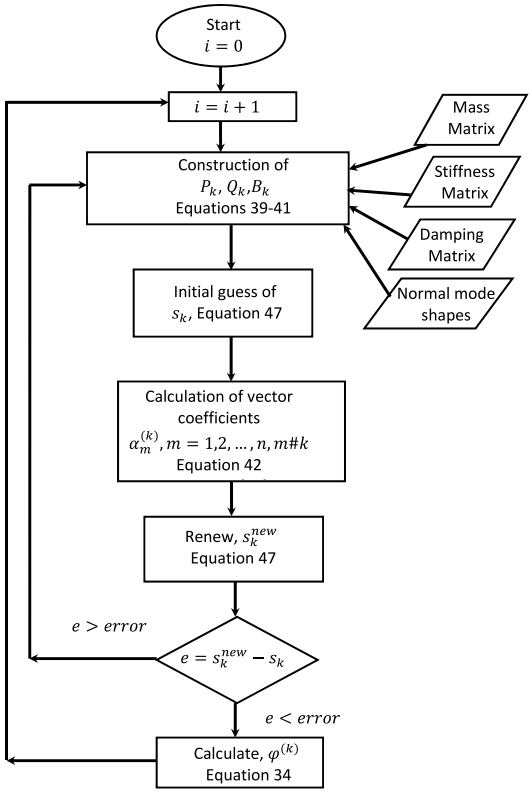

Fig. 4. Algorithm for calculation of complex mode shapes.

results show that, from the fixed end, the phase angle increases close to the area of damage to a maximum positive value just before this area and then rapidly decreases through the damaged area reaching a minimum just beyond and then tending to a value close to zero near the free end. The maximum amplitude of the phase angle change increases with level of damage giving a value of 1.58° for DIL=9.

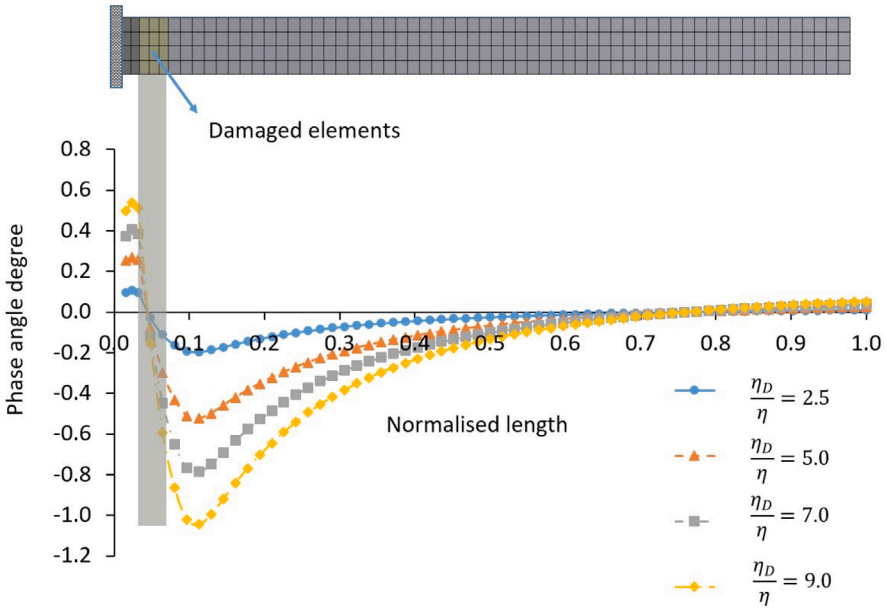

Fig. 5. Phase angle of motion of the structural elements for the first bending mode for Damage Case 1. The damaged area is shown by the shaded region. The specimen is fixed on the left hand side.

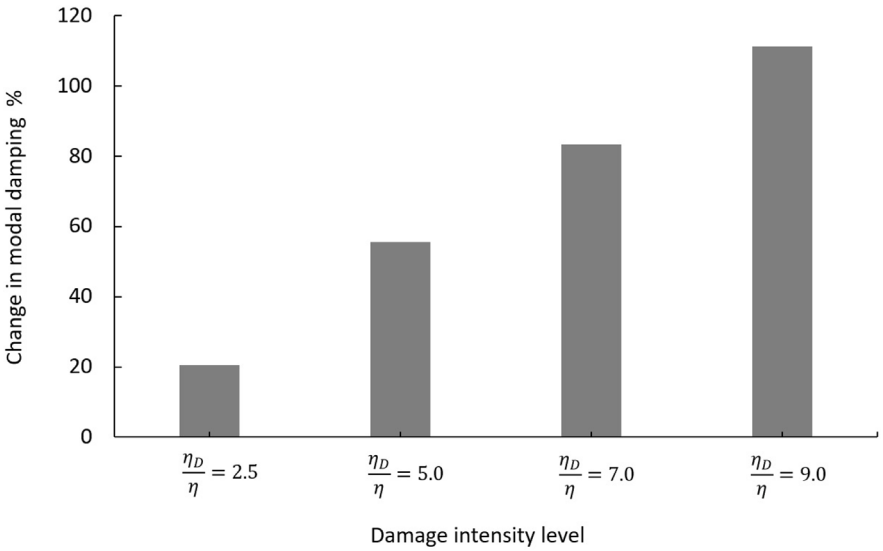

Fig. 6. Variation of modal damping for Damage Case 1 for different DILs.

The effect of local damage on the modal damping of the whole specimen is shown in Fig. 6. The change in modal damping varies from 22.3% for DIL=2.5 to 110% for DIL=9.

The effect of damage on the phase angle of motion of the structural elements for the first mode shape for Damage Case 2 for different DILs is shown in Fig. 7. The pattern of variation in the phase angle is similar to Damage Case 1, with the maximum peak shifted further away from the fixed end close to the area of damage. The maximum difference in phase for the same DIL=9 is reduced significantly from 1.5° in Damage Case 1 to 0.55° in this case. For this DIL, the change in modal damping also reduces from 110% in Damage Case 1 to 88% relative to an undamaged specimen as shown in Fig. 8.

To better localize damage, the spatial derivative of the phase angle for the first bending mode for DIL=9 is calculated and the results shown in Fig. 9. It can be seen that the derivative becomes increasingly negative around the damaged elements reaching a minimum value within the area of damage. The results for other DILs are not shown but show a similar pattern.

For all four damage cases, the phase angles are plotted for DIL=9 in Fig. 10.

The magnitude of the phase angle change reduces significantly as the damaged section moves away from the fixed end. This is logical for the first mode shape as local strains progressively reduce moving away from the fixed end and therefore the dissipation of energy is less. This effect can also be observed when analysing the modal damping of the specimen for the four damage cases as shown in Fig. 11 where the change in modal damping reduces from 110% in Damage Case 1 to 19.8% in Damage Case 4.

4.2. *Effect of damage on different mode shapes*

In cantilever beam-type structures, the mode with dominant elastic energy, which is the first bending mode, affects the phase angle the most. Therefore, the first bending mode would normally be expected to be the most appropriate mode to consider for the localization of

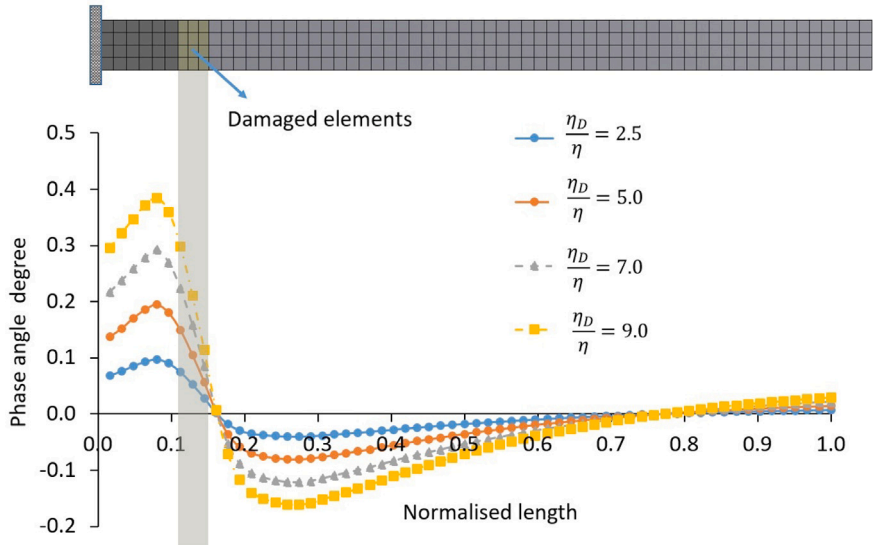

Fig. 7. As Fig. 5 but for Damage Case 2.

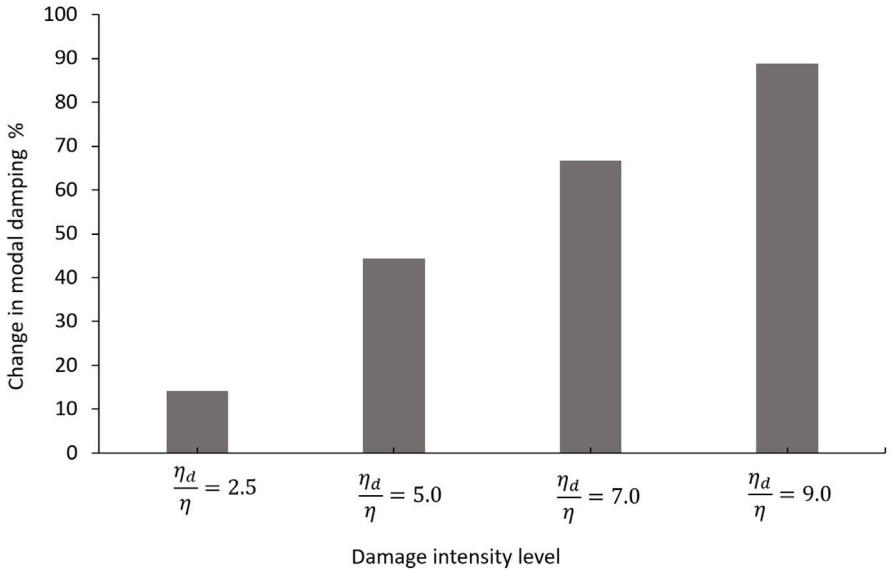

Fig. 8. Variation of the modal damping for Damage Case 2 for different DILs.

damage. However, the elastic energy in this mode decreases when moving from the fixed end to the free end. So if the damage is some distance from the fixed end, it cannot be detected by the first mode. The second mode has a similar elastic energy distribution as the first mode and also may not be the most convenient for detecting damage away from the fixed end. The most appropriate mode shape in this case to detect the damage is the third mode. This has a node close to the area of damage where the elastic energy within the structural elements close to the node is high.

The effect of damage on the phase angle of motion of the structural elements for the third bending mode for Damage Case 4 for different DILs is shown in Fig. 12 for part of the specimen. The third bending mode shape has a node (the point on the structure without any movement) at structural element 32 as shown in the inset to Fig. 12. The damaged area in this case is located far from the fixed end and closer to the structural element where the levels of strain are relatively high. This leads to higher local levels of energy dissipation and a larger change in the phase angle close to the area of damage compared to the first bending mode. For DIL=9, the maximum change in phase angle is now around 0.4° compared with only 0.1° for the first bending mode. It should be noted that Fig. 12 shows the phase angle for only part of the specimen as, in the areas around the node where displacements are very small, the phase angle and its derivative become invalid due to division by a very small number. The resulting discontinuities can be seen in Fig. 13 which shows the phase angle for the entire specimen.

The modal damping of the specimen for the third bending mode for Damage Case 4 at different DILs is shown in Fig. 14. It can be seen that at DIL η_d/η=9, the increase in modal damping is about 25% which is higher compared with the first bending mode (19.8%).

The spatial derivative of the phase angle for the third bending mode is shown in Fig. 15. This is shown for DIL η_d/η=9 but similar results are seen for other DIL values. It can be seen from Fig. 15 that the location of the damage is where the derivative of the phase angle shows a minimum.

It seems that derivatives of nodal phase angle is a useful parameter to localize damage although the large value near the structure node could be misleading due to overestimating of this value near to the structure node.

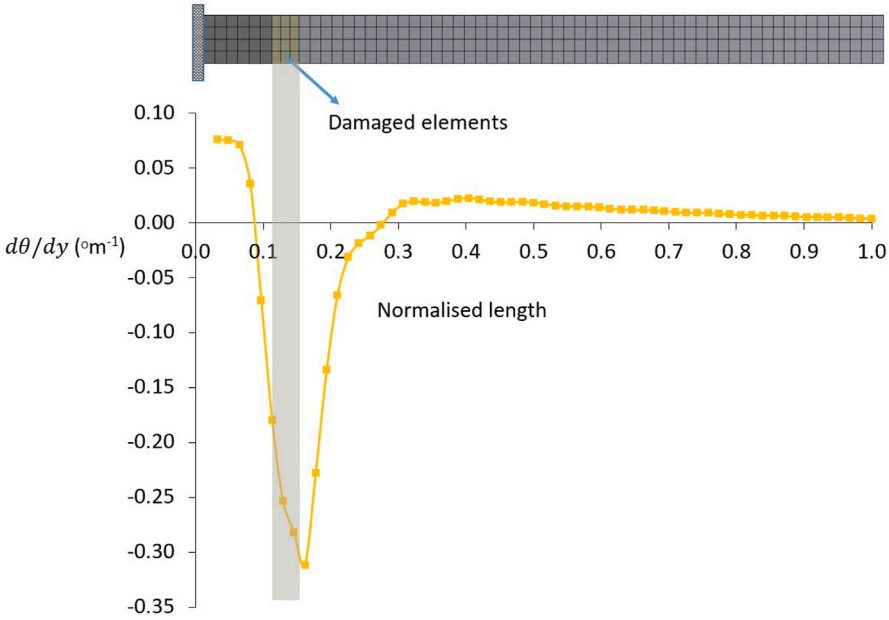

Fig. 9. Derivative of the phase angle for the first bending mode for DIL=9.

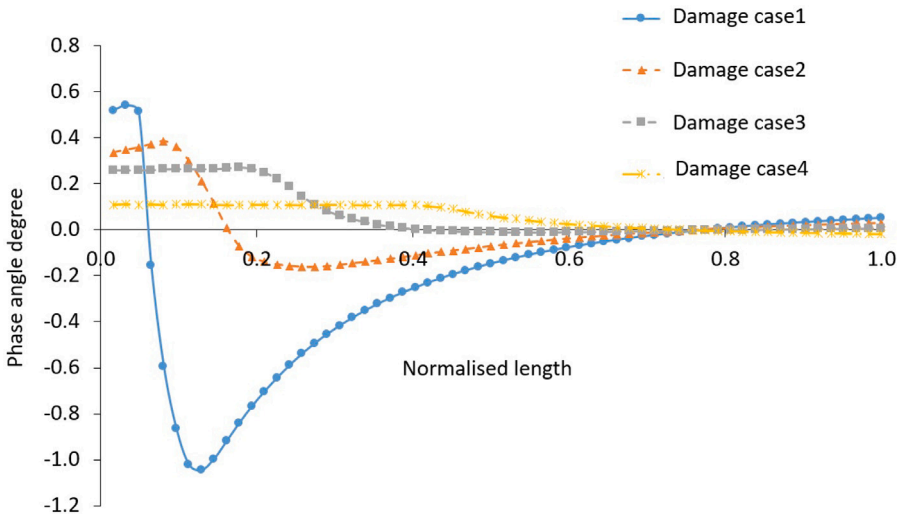

Fig. 10. Phase angle of motion of the structural elements for the first bending mode for different damage locations for DIL=9.

4.3. Sensitivity to the size of the damaged area

To look at the effect of the size of the damaged area on the maximum change in the phase angle of the mode shape, three different areas of damage for Damage Case 1 with DIL=9 were considered. For a damaged area equal to 4% of the total area of the test specimen, the maximum change in the phase angle of the first bending mode was 1.58°. For damaged areas equal to 2.6% and 1.3% of the total area of the test specimen, the maximum changes in the phase angle of the first bending mode were equal to 0.975° and 0.371°, respectively. The ability to measure such changes in phase angle in a real specimen is difficult to determine, but this analysis at least gives an indication of the size of change that would be expected.

4.4. Effect of damage on resonant frequency and mode shape

Based on a previous experimental study [19], the change in material stiffness is small during damage progression compared with damping. Therefore, the stiffness of the damaged sections was considered unchanged in this model, and only damping assumed to have increased. This means that the natural frequencies for all damaged cases are the same and there is a negligible change in resonant frequencies due to damping. The first mode resonant frequency for the healthy specimen is 49.272 Hz, and in Damage Case 1 with DIL=9, the resonant frequency is 49.321 Hz. The mode shapes are effectively the same, with very small changes around the damaged region that cannot be distinguished by Modal Assurance Criterion (MAC) values. The phase angle of the mode shape changes for the worst case scenario (Damage Case 1 and DIL=9) from 0.539 degrees to −1.05 degrees, with cosine values of 0.99995 and 0.99983 respectively, which gives a MAC value very close to 1 (0.9999996).

5. Discussion

From the modal analysis, the time-dependent displacement of the structure is determined based on measurements from appropriate motion sensors. This time-displacement response is then used to determine

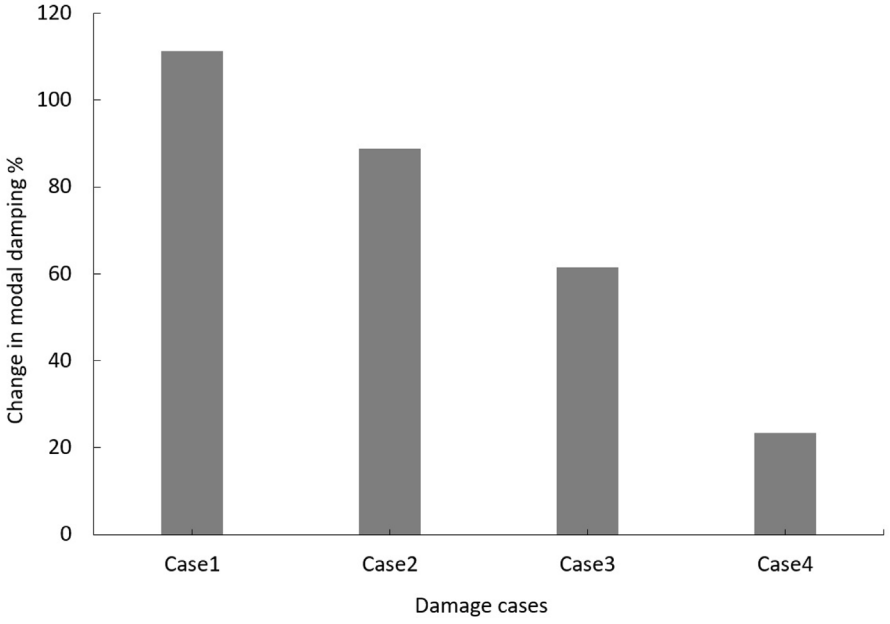

Fig. 11. Modal damping of the first bending mode for the different damage cases and a DIL η_d/η=9.

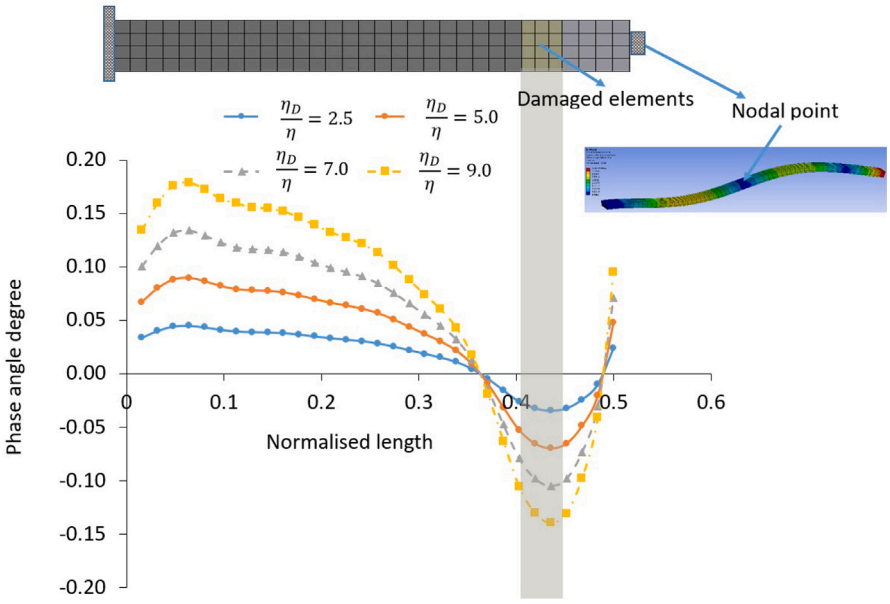

Fig. 12. Phase angles of the third bending mode for Damage Case 4 for different DILs.

the frequency response function (FRF) of the structure. In this section, it is shown that the phase of the diagonal components of the FRF is related to the phase at the locations of the structural elements for a given mode shape. This is a method that can be used to determine experimentally the phase angle of the motion of the structural elements for a given mode shape.

The FRF has n degrees of freedom and is a $n \times n$ matrix. Each component of the FRF has a magnitude and phase which are dependent on the frequency. The phase of the FRF at the resonant frequency for a specific excitation mode in a healthy structure is 90° as the damping is almost proportional throughout the entire structure. When local damage occurs in the structure, the damping is no longer proportional, the mode shapes become complex and the phases of motion of the structural elements of the FRF at resonant frequency are no longer 90°.

The damping matrix in a viscoelastic damping model of the structure is dependent on the frequency (see Eq. (21)). Because we are interested in the response of the structure in a narrow band around the resonant frequency, the damping matrix can be considered constant in this narrow band and equal to its value at the resonant frequency. With this assumption, the diagonal components of the FRF at the kth resonant frequency ($\omega_{k,res}$) can be written as [25]:

$$\mathrm{FRF}_{i,i}(\omega = \omega_{k,res}) = \frac{\phi_i^{(k)}\phi_i^{(k)}}{m_k(\lambda_k^2 - (\omega_{k,res})^2)} + \sum_{q=1,q\neq k}^{n} \frac{\phi_i^{(q)}\phi_i^{(q)}}{m_q(\lambda_q^2 - (\omega_{k,res})^2)} \tag{48}$$

Where $\phi_i^{(k)}$ is the ith component of the kth complex displacement mode shape and $\omega_r^{(k)}$ is the kth resonant frequency. The index q refers to the different displacement mode shapes, other than the kth mode shape. The modal mass of the kth mode shape is defined as:

$$m_k = (\phi^{(k)})^T \boldsymbol{M}\, \phi^{(k)} \tag{49}$$

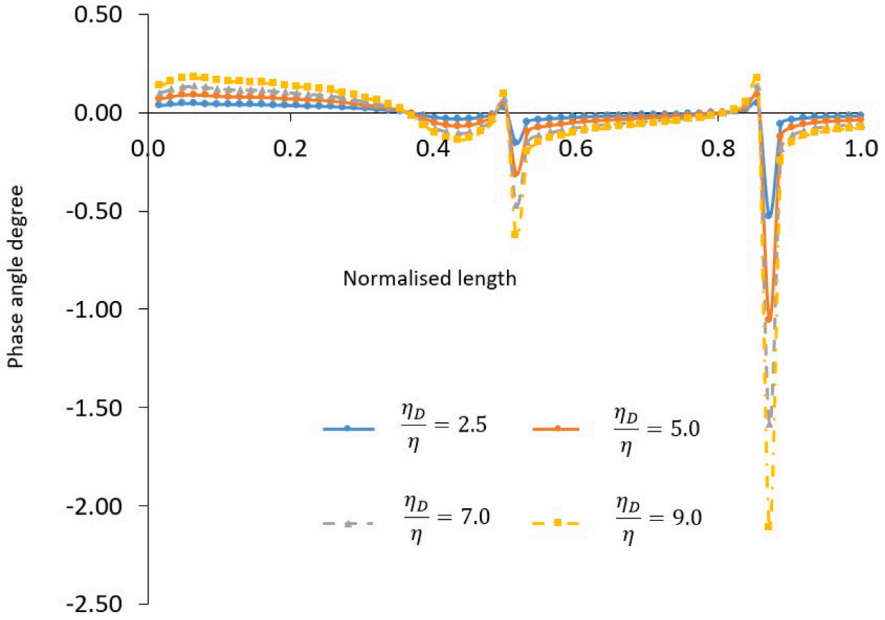

Fig. 13. As Fig. 12, but showing the phase angle for the whole length of the test specimen.

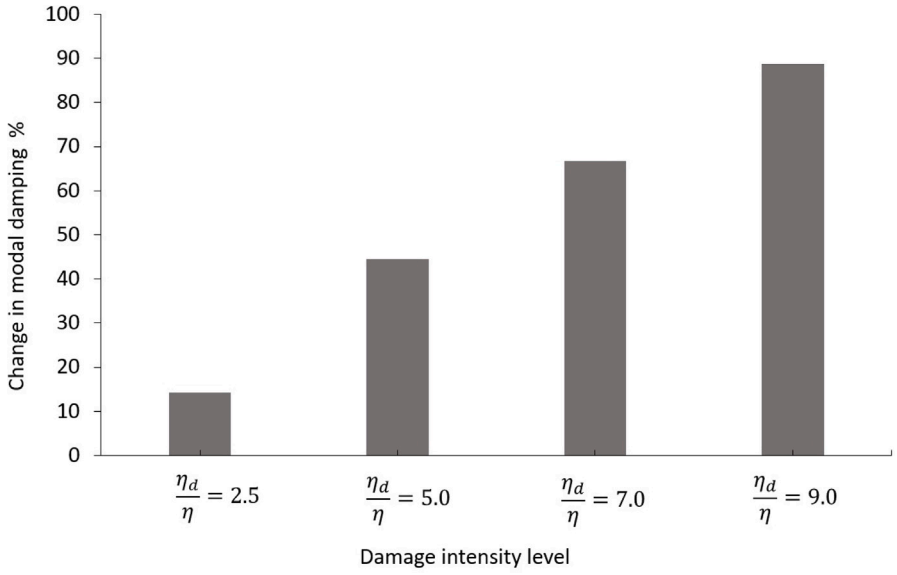

Fig. 14. Variation in modal damping for the third bending mode for Damage Case 4 and different DILs.

The resonant frequency $\omega_{k,res}$ is the frequency of the structure where the amplitude of the FRF components are greatest. From Eq. (48), this maximum amplitude occurs when the denominator is minimized.

This occurs when the kth resonant frequency is equal to:

$$\omega_{k,res} = \omega_k \sqrt{1 - 2\zeta_k^2} \tag{50}$$

The FRF at the kth resonant frequency, to a good approximation, can be estimated by neglecting the effect of the second term in Eq. (48) [25]. Neglecting the second term and substituting Eq. (28) and (50) into Eq. (48) then:

$$\mathrm{FRF}_{i,i}(\omega = \omega_{k,res}) = \frac{\|\phi_i^{(k)}\|^2 e^{2j\theta_i^{(k)}}}{j(2m_k\omega_k^2\zeta_k\sqrt{1-\zeta^2})} \tag{51}$$

The phase of the diagonal components of the FRF at the kth resonant frequency can be written as:

$$\mathrm{Arg}(\mathrm{FRF}_{i,i}(\omega = \omega_{k,res})) = \mathrm{Arg}(\|\phi^{(k)}\|^2 e^{j2\theta_i^{(k)}}) - \mathrm{Arg}(j(2\omega_k^2\zeta_k\sqrt{1-\zeta^2})) - \mathrm{Arg}(m_k) \tag{52}$$

The phase of the first term in Eq. (52) is equal to $2\theta_i^{(k)}$ and the phase of the second term is equal to 90^0. For simplicity, $\mathrm{Arg}(\mathrm{FRF}_{i,i}(\omega = \omega_{k,res}))$ is replaced by $\beta_{i,i}^{(k)}$ and then Eq. (52) can be written as (assuming all angles in degrees):

$$\beta_{i,i}^{(k)} = 2\theta_i^{(k)} - \mathrm{Arg}(m_k) - 90° \tag{53}$$

When there is no damage, damping is proportional and $\theta_i^{(k)}$ is zero and the modal mass is a real number so its arguments are also zero and therefore the phase of the ith component of the FRF at the kth resonant frequency is $-90°$ as expected.

When there is local damage, $\theta_i^{(k)}$ is no longer zero and the modal mass of the kth mode shape is a complex number. The modal mass is an overall property of the structure and is dependent on the mass matrix and mode shape. Therefore, local damage does not have much influence on this parameter or its phase. This can be seen by considering the

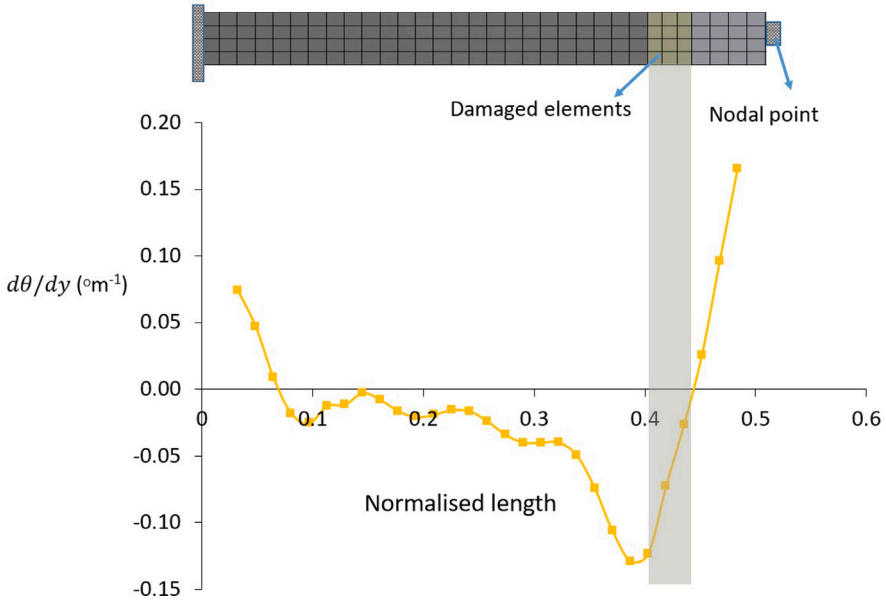

Fig. 15. Derivative of the phase angle for the third bending mode at DIL $\eta_d/\eta = 9$.

phase of the modal mass in this study at DIL= 9 and at the first resonant frequency ((ω_1 = 49.32 Hz) which is equal to 0.0000435°. Therefore, Eq. (53) can be written as:

$$\beta_{i,i}^{(k)} \approx 2\theta_i^{(k)} - 90° \tag{54}$$

This equation relates the phase of the motion of the structural components for a particular mode shape to the phase of the diagonal components of the FRF.

6. Conclusion

A new indicator for the localization of fatigue damage in a fibre glass composite material, *i.e.,* the thick adhesive joint of a wind turbine blade is presented. The indicator analyses the change in the phase of mode shapes of the structural elements to localize damage.

Using a well-known finite element structural code, the results show that this approach can effectively localize simulated damage, though the phase changes observed are relatively small, which may be challenging to detect in practice. In the case of a real wind turbine blade, aerodynamic damping will play a role though this is more likely to affect the global movement of the blade rather than the relative movement of localized elements. It is this relative change that is the important factor in damage detection. Nevertheless, it would require further work to assess its impact on the ability to detect damage using the proposed indicator.

The change in the phase of mode shape of the structural elements depends on the location of damage and detecting damage in locations with less strain energy is more challenging than in other locations where the level of strain is higher. Therefore, the selection of the most appropriate mode shapes to use for this method plays an important role in the localization of damage.

In a practical measurement system, the phase angle of each structural element should be obtained from the FRF. For this indicator to be used, the spatial change in phase angle should be measured at a few key positions. Installing vibration sensors at relatively few locations on a blade would be sufficient based on a finite element study to determine the relevant mode shapes although damage localization accuracy may be limited.

To have good accuracy in measuring the change in phase angle of mode shapes, a relatively large number of sensors would be required. Increasing the number of sensors adds complexity when installing a monitoring system, however, by using fibre optic sensor technology this is not insurmountable. In addition, the use of ground-based or airborne remote laser scanning technology could be a future solution to be used in periodic inspection. It should be stressed that the purpose of this paper was merely to establish the ability to use changes in damping properties as a way of detecting damage. Clearly, further work is required to develop an operational measurement system. The overall dimensions of the structure and the relative size of adhesive layer to laminate thickness will affect the potential change in phase angles during damage initiation. However, the purpose of this work was to provide a proof of concept which would require further research and refinement in a real world situation.

CRediT authorship contribution statement

S. Khoshmanesh: Conceptualization, Methodology, Formal analysis/modeling, Interpretation of data, Validation, Writing – original draft, Writing – review & editing, Project administration. **S.J. Watson:** Conceptualization, Methodology, Interpretation of data, Validation, Writing – review & editing, Supervision, Project administration. **D. Zarouchas:** Conceptualization, Methodology, Interpretation of data, Validation, Writing – review & editing, Supervision, Project administration.

Declaration of competing interest

The authors declare that they have no known competing financial interests or personal relationships that could have appeared to influence the work reported in this paper.

Data availability

Data will be made available on request.

References

[1] Yang Wenxian, Tavner Peter J, Crabtree Christopher J, Feng Y, Qiu Y. Wind turbine condition monitoring: technical and commercial challenges. Wind Energy 2012;17(5):673–93. http://dx.doi.org/10.1002/we.1508, https://doi.org/10.1002/we.1508.

[2] Hu B, Stumpf P, van der Deijl W. Offshore wind access. TNO report, Report no: R10633, 3rd ed. 2019.

[3] Coronado Diego, Fischer Katharina. Condition monitoring of wind turbines: State of the art , user experience and recommendations project report. 2015.
[4] Li Dongsheng, Ho Siu-Chun M, Song Gangbing, Ren Liang, Li Hongnan. A review of damage detection methods for wind turbine blades. Smart Mater Struct 2015;24(3):033001. http://dx.doi.org/10.1088/0964-1726/24/3/033001, https://doi.org/10.1088/0964-1726/24/3/033001.
[5] Carden E Peter, Fanning Paul. Vibration based condition monitoring: A review. Struct Health Monit 2004;3(4):355–77. http://dx.doi.org/10.1177/1475921704047500, https://doi.org/10.1177/1475921704047500.
[6] Montalvao D. A review of vibration-based structural health monitoring with special emphasis on composite materials. Shock Vib Dig 2006;38(4):295–324. http://dx.doi.org/10.1177/0583102406065898, https://doi.org/10.1177/0583102406065898.
[7] Farrar R, Francois H, Devin S, Daniel W, Stinemates R, Jerry C. A review of structural health monitoring literature: 1996–2001. University of North Texas Libraries, UNT Digital Library; 2002.
[8] Doebling SW, Farrar CR, Prime MB. A summary review of vibration-based damage identification methods. Shock Vib Dig 1998;30(2):91–105. http://dx.doi.org/10.1177/058310249803000201, https://doi.org/10.1177/058310249803000201.
[9] Al-Khudairi Othman, Hadavinia Homayoun, Little Christian, Gillmore Gavin, Greaves Peter, Dyer Kirsten. Full-scale fatigue testing of a wind turbine blade in flapwise direction and examining the effect of crack propagation on the blade performance. Materials 2017;10(10):1152. http://dx.doi.org/10.3390/ma10101152, https://doi.org/10.3390/ma10101152.
[10] Modena Claudio, Sonda D, Zonta Daniele. Damage localization in reinforced concrete structures by using damping measurements. Key Eng Mater 1999;167–168:132–41. http://dx.doi.org/10.4028/www.scientific.net/kem.167-168.132, https://doi.org/10.4028/www.scientific.net/kem.167-168.132.
[11] Zonta D, Modena C. Observations on the appearance of dispersive phenomena in damaged structures. J Sound Vib 2001;241(5):925–33. http://dx.doi.org/10.1006/jsvi.2000.3320, https://doi.org/10.1006/jsvi.2000.3320.
[12] Kawiecki Grzegorz. Modal damping measurement for damage detection. Smart Mater Struct 2001;10(3):466–71. http://dx.doi.org/10.1088/0964-1726/10/3/307, https://doi.org/10.1088/0964-1726/10/3/307.
[13] Keye S, Rose M, Sachau D. Localizing delamination damages in aircraft panels from modal damping parameters. In: Proc. 19th international modal analysis conf. 2001, p. 412–7.
[14] Montalvão D, Ribeiro AMR, Duarte-Silva J. A method for the localization of damage in a CFRP plate using damping. Mech Syst Signal Process 2009;23(6):1846–54. http://dx.doi.org/10.1016/j.ymssp.2008.08.011, https://doi.org/10.1016/j.ymssp.2008.08.011.
[15] Treviso A, Van Genechten B, Mundo D, Tournour M. Damping in composite materials: Properties and models. Composites B 2015;78:144–52. http://dx.doi.org/10.1016/j.compositesb.2015.03.081, https://doi.org/10.1016/j.compositesb.2015.03.081.
[16] Gibson Ronald F. Damping characteristics of composite materials and structures. J Mater Eng Perform 1992;1(1):11–20. http://dx.doi.org/10.1007/bf02650027, https://doi.org/10.1007/bf02650027.
[17] Zarouchas DS, Makris AA, Sayer F, Van Hemelrijck D, Van Wingerde AM. Investigations on the mechanical behavior of a wind rotor blade subcomponent. Composites B 2012;43(2):647–54. http://dx.doi.org/10.1016/j.compositesb.2011.10.009, https://doi.org/10.1016/j.compositesb.2011.10.009.
[18] Sayer Florian, Antoniou Alexandros, van Wingerde Arnoldus. Investigation of structural bond lines in wind turbine blades by sub-component tests. Int J Adhes Adhes 2012;37:129–35. http://dx.doi.org/10.1016/j.ijadhadh.2012.01.021, https://doi.org/10.1016/j.ijadhadh.2012.01.021.
[19] Khoshmanesh S, Watson SJ, Zarouchas D. The effect of the fatigue damage accumulation process on the damping and stiffness properties of adhesively bonded composite structures. Compos Struct 2022;287:115328. http://dx.doi.org/10.1016/j.compstruct.2022.115328, https://doi.org/10.1016/j.compstruct.2022.115328.
[20] Barbero Ever J. Finite element analysis of composite materials. CRC Press; 2007.
[21] McTavish DJ, Hughes PC. Modeling of linear viscoelastic space structures. J Vib Acoust 1993;115(1):103–10. http://dx.doi.org/10.1115/1.2930302, https://doi.org/10.1115/1.2930302.
[22] Lakes Roderic, Lakes Roderic S. Viscoelastic materials. Cambridge University Press; 2009.
[23] Sørensen Bent F, Holmes John W, Brøndsted Povl, Branner Kim. Blade materials, testing methods and structural design. In: Wind power generation and wind turbine design. WIT Press; 2010, p. 417–65. http://dx.doi.org/10.2495/978-1-84564-205-1/13, https://doi.org/10.2495/978-1-84564-205-1/13.
[24] Mishnaevsky Leon, Branner Kim, Petersen Helga, Beauson Justine, McGugan Malcolm, Sørensen Bent. Materials for wind turbine blades: An overview. Materials 2017;10(11):1285. http://dx.doi.org/10.3390/ma10111285, https://doi.org/10.3390/ma10111285.
[25] Ewins David J. Modal testing: Theory, practice and application. John Wiley & Sons; 2009.
[26] Brincker Rune, Ventura Carlos. Introduction to operational modal analysis. John Wiley & Sons; 2015.
[27] Woodhouse J. Linear damping models for structural vibration. J Sound Vib 1998;215(3):547–69. http://dx.doi.org/10.1006/jsvi.1998.1709, https://doi.org/10.1006/jsvi.1998.1709.
[28] Adhikari Sondipon. Structural dynamic analysis with generalized damping models: Analysis. John Wiley & Sons; 2013.